

Electronic regulation of Ni single atom by confined Ni nanoparticles for fast and energy-efficient CO₂ electroreduction

Wenhao Ren

École polytechnique fédérale de Lausanne

Xin Tan

Australian National University

Chen Jia

UNSW Sydney

Anna Krammer

École polytechnique fédérale de Lausanne

Qian Sun

UNSW Sydney

Jiangtao Qu

University of Sydney <https://orcid.org/0000-0003-0357-4205>

Sean Smith

Australian National University

Andreas Schueler

École polytechnique fédérale de Lausanne

Xile Hu

École Polytechnique Fédérale de Lausanne <https://orcid.org/0000-0001-8335-1196>

Chuan Zhao (✉ chuan.zhao@unsw.edu.au)

UNSW Sydney <https://orcid.org/0000-0001-7007-5946>

Article

Keywords: energy efficiency, electroreduction, Ni single-atom, electrocatalysis

Posted Date: September 25th, 2021

DOI: <https://doi.org/10.21203/rs.3.rs-850267/v1>

License: © ⓘ This work is licensed under a Creative Commons Attribution 4.0 International License.

[Read Full License](#)

Abstract

Electrocatalytic CO₂ to CO conversion is approaching the industrial benchmark. Currently, Au electrodes show the best performance, whereas non-precious metal catalysts exhibit inferior activity. Here we show a densely populated Ni single-atom on nanoparticle catalyst (NiSA/NP) via direct solid-state pyrolysis, where Ni nanoparticles donate electrons to Ni(i)-N-C sites via carbon nanotubes network, achieves a high CO current of 352 mA cm⁻² at -0.55 V vs RHE in an alkaline flow cell. When coupled with a NiFe-based oxygen evolution anode into a zero-gap membrane electrolyser, it delivers an industrial-relevant CO current of 310 mA cm⁻² at a low cell voltage of -2.3 V, corresponding to an overall energy efficiency of 57%. The superior CO₂ electroreduction performance is attributed to the enhanced adsorption of key intermediate COOH* on electron-rich Ni single atom, together with the dense active sites.

Introduction

Electrochemical CO₂ reduction reaction (CO₂RR) emerges as a carbon-neutral approach to recycle CO₂ and store intermittent renewable energies.¹⁻⁴ However, the chemical inertness of CO₂ molecule and its multiple reaction pathways with up to 16 possible products cause electrocatalytic conversion processes energy-inefficient.^{5,6} To achieve scalability for the technology, the reaction must occur at industrial-level currents at low overpotentials for ideally a single product. Currently, electrolyzers for CO₂ conversion to CO are reaching the pilot scale,^{7,8} of which Au and Ag are the most promising catalysts.⁹ Based on the membrane electrode assembly (MEA) device, certain Au/IrO₂ full cell has achieved a CO current density of 300 mA cm⁻² at a cell voltage of ~ 2.65 V.¹⁰ According to the industrial benchmarks for CO₂-to-CO electrolysis proposed in 2021, there remains a big gap to achieve higher current densities (> 400 mA cm⁻²) at the lower cell voltages (< 2.5 V), by using non-precious metal catalysts.⁷

Single-atom catalysts (SACs) with metal-N-C (Fe, Co, Ni, etc.) structures have demonstrated promising performance for CO₂ conversion.¹¹ Gu et al. have developed an atomically dispersed Fe³⁺-N-C site that can deliver a CO partial current density of 94 mA cm⁻² at an overpotential of 340 mV.¹² Certain self-supported Ni-N-C membrane catalysts can produce CO with a high current of 308.4 mA cm⁻² and 88% Faradaic efficiency (FE) in a flow cell.¹³ Despite these breakthroughs, their single-atom nature with homogeneously dispersed active sites are only efficient in catalyzing single-molecule conversions.¹⁴ For complex reactions that involve multiple intermediates, they generally show either too strong or too weak binding to one or more intermediates due to the scaling relationship.¹⁵ For example, Ni-N-C sites typically exhibit very weak binding to COOH* while Fe-N-C sites exhibit too strong binding to CO*, both of which hinder efficient CO production.¹⁶ Besides, the very low metal loading of SACs also severely limits their activity for practical applications.

Here, we show a cooperative Ni single-atom-on-nanoparticle catalyst (NiSA/NP) for energy-efficient CO₂ electroreduction. The design of this hybrid SAC enables: (i) electron density regulation of surface Ni-N-C

Loading [MathJax]/jax/output/CommonHTML/jax.js

by the encapsulated Ni nanoparticles for faster intermediate adsorption and desorption; (ii) *in situ* growth of high loading Ni single atoms on carbon nanotubes (CNTs) fed by Ni nanoparticles; (iii) a simple and scalable method for the mass synthesis of Ni SACs. The NiSA/NP catalyst achieves state-of-the-art CO₂-to-CO performance in both the H-cell and zero-gap MEA full cells.

Results

Catalyst design and DFT prediction. Most of Ni-N-C catalysts have been revealed to show very weak binding to COOH* intermediate upon CO₂-to-CO conversion.^{13,16} Therefore, injecting foreign electrons into Ni single atom to tune its d band structure is desirable for enhancing the adsorption of COOH*. Based on this principle, previous studies have found that Ni(i)-N-C shows significantly enhanced CO₂RR activity compared to Ni(ii)-N-C.¹⁷ Note that metal nanoparticles can be easily formed with single atoms because of the aggregation effect, and the formation of nanoparticles sometimes is inevitable if a high loading of single atom is pursued. In this case, the electron-rich structure of metal nanoparticles can potentially tune the electronic configuration of nearby metal-N-C,¹⁸ and enhance its electrocatalytic performance. Given that Ni is a strongly interacting metal with carbon,¹⁹ we propose a Ni-N-C on Ni nanoparticles design, and firstly use DFT calculations to predict the electron distribution and charge transfer between Ni nanoparticles and a layer of graphene via the deformation electronic density calculation and Bader analysis. Here face-centered cubic Ni(111) is used as the targeted model because of its lowest formation energies among the different phases.²⁰ As shown in Fig. 1a,b, the first layer of Ni(111) can easily bind with the adjacent carbon, which leads to a total transfer of 2.45 e⁻ to the carbon surface.

We next shift our attention to study the effects of extra electrons on the Ni-N-C structures for CO₂RR. Here, two representative structures including coordinatively saturated NiN₄ (Fig. S1) and unsaturated NiN₃V are considered (Fig. S2),^{13,21,22} where V stands for vacancy and Ni single atom is the active site.²³ COOH* and CO* are intermediates for electrochemical CO₂-to-CO conversion.²⁴ On neutral Ni-N-C catalysts, as shown in Fig. 1c,d, the rate-limiting steps are CO₂(g)→COOH* on both NiN₄ and NiN₃V with the overpotential of 1.50 V and 0.84 V, respectively, attributed to the weak binding of COOH* on NiN₄ and NiN₃V. After injecting extra electrons into the Ni-N-C structure, the binding strength of COOH* and CO* on NiN₄ and NiN₃V are greatly enhanced with the increase of extra electrons. In comparison with the neutral cases, the stronger binding of COOH* on negatively charged NiN₄ and NiN₃V reduces the overpotential of CO₂RR and enhances their activities. To understand the effects of extra electrons on the enhanced binding strength of COOH* and CO* on Ni-N-C, we then calculated the number of electrons localized on Ni single atom (Fig. 1e). The results show that the number of electrons on Ni atom increases with the injected extra electrons on Ni-N-C. More electrons localized on Ni single atom results in stronger binding of intermediates compared to those on neutral cases.

Given that hydrogen evolution reaction (HER) is a dominant side reaction that is competitive with the CO₂RR, we calculate the difference between thermodynamic limiting potentials for CO₂RR and HER

Loading [MathJax]/jax/output/CommonHTML/jax.js

(denoted as $UL(CO_2)-UL(H_2)$), which can reflect the selectivity (Fig. S4).^{25,26} Fig. 1f shows the $UL(CO_2)-UL(H_2)$ on negatively charged NiN_4 and NiN_3V , in comparison with the neutral cases. Clearly, negatively charged NiN_4 and NiN_3V show more positive values of $UL(CO_2)-UL(H_2)$, corresponding to their higher selectivity for CO production.

Catalysts synthesis and characterizations. We pursued the nanoparticle co-catalysis effect experimentally by one-step solid-state pyrolysis with excessive Ni sources. The schematic diagram of the catalyst design and formation mechanism is shown in Fig. S5a. First, the melamine was decomposed into carbon nitride at $\sim 400^\circ C$.²⁷ With the increase of annealing temperature, the Ni nanoparticles catalyzed the carbon nitrite to generate the carbon nanotubes (CNTs),²⁸ meanwhile Ni single atoms were trapped by the nitrogen-doped CNTs via thermal emitting.^{29,30} The NiSA/NP was obtained after the heat treatment followed by the acid washing to remove the Ni nanoparticles outside of CNTs. Figure 2a shows the morphology of the NiSA/NP catalyst, where large amounts of Ni nanoparticles are confined inside of the nitrogen-doped CNTs. The EDS mapping confirms the presence of Ni and N in the carbon matrix, and evenly distributed Ni nanoparticles at micron-scale (Fig. S5d). The bright dots displayed in Fig. 2b are assigned to the Ni single atoms anchored on CNTs. For comparison, pure NiSA was prepared by the treatment of NiSA/NP with NH_4Cl to remove Ni nanoparticles inside of the CNTs.³¹ As confirmed by TEM (Fig. 2c and Fig. S6) and X-ray diffraction (XRD, Fig. 2d), most of the Ni nanoparticles inside of CNTs were removed after the NH_4Cl treatment while Ni single atoms remained. XRD also shows a dominant Ni(111) peak of the catalysts which is consistent with the DFT modelling. The XPS N 1s spectra of NiSA and NiSA/NP exhibit similar pyridinic (398.5 eV), pyrrolic (401.2 eV), graphitic (402.7 eV), and Ni-N (399.4 eV) peaks (Fig. S7b,c), indicative of the identical Ni-N-C structure after the removal of Ni nanoparticles. According to the ICP-OES, the Ni contents in NiSA/NP and NiSA are 8.8 wt% and 4.6 wt%, respectively. The high content of Ni single atom can be attributed to (i) the *in-situ* formation of Ni-N-C during the growth of CNTs and (ii) the excessive Ni sources provided by the Ni nanoparticles.

The unpaired electron in catalysts was directly observed by EPR spectroscopy (Fig. 2e), where a g -value of 2.17 is obtained for both samples and could be assigned to the unpaired electron in the $3d_{x^2-y^2}$ orbital of Ni(i).^{32,33} The EPR signal intensity of NiSA/NP is above 2 times higher than NiSA, corresponding to the electron-rich structure due to the presence of Ni nanoparticles, consistent with the Bader analysis. We further examined the d band structure of Ni using ultraviolet photoelectron spectroscopy (UPS, Fig. 2f and Fig. S8). No obvious metallic Ni peak can be observed across the Fermi level, which can be attributed to the fully confined Ni nanoparticles inside of CNTs that exceeded the detection limit of UPS (2–3 nm), in line with XPS results (Fig. S7a). Therefore, the shift of near Fermi level signals (0–1 eV) can be attributed to the change of electronic structure of Ni single atoms on the surface of CNTs. The position of NiSA increases in binding energy compared to NiSA/NP (away from the Fermi level). According to d band theory, the downshifted d band of NiSA (grey curve) corresponds to a weakened adsorption strength,³⁴ which is in good accordance with DFT calculation.

The Ni K-edge X-ray absorption near-edge structure (XANES) and extended X-ray absorption fine structure (EXAFS) measurements were carried out to identify the electronic structure and coordination environment of catalysts. Ni foil and NiPc were used as references for metallic Ni and Ni²⁺, respectively. The pre-edge curve of NiSA sites between Ni foil and NiPc (Fig. 2g), suggesting a valence state of Ni⁺.³⁵ Ni(i)-N-C has been revealed as a highly active site for CO₂-to-CO conversion.³² More importantly, the pre-edge position of NiSA/NP is between the Ni foil and NiSA, corresponding to an even lower average valence state than Ni⁺. The Fourier-transformed k³-weighted spectra of the samples exhibit two major peaks at 1.45 Å and 2.1 Å, which are assigned to Ni-N and Ni-Ni coordination shells, respectively (Fig. 2h). The significantly decreased Ni-Ni peak intensity in NiSA compared with NiSA/NP corresponds to the removal of Ni nanoparticles. Note that the Ni-Ni peak can be easily observed even there are only residual Ni NPs in the catalysts.³¹ Based on the EXAFS fitting of Ni-N shell on NiSA, the coordination number is determined to be 2.7 which is close to the coordinative unsaturated NiN₃V structure (Fig. 2i and Table S2).

Electrochemical CO₂ conversion. The electrochemical testing was firstly conducted in an H-cell using 0.5 M KHCO₃ electrolyte and the corresponding calibration curve is shown in Fig. S9. Figure 3a displays the partial CO currents at different potentials, where the NiSA/NP outperforms the NiSA in a wide potential window, achieving a high current of 131 mA cm⁻² at -1.0 V vs RHE which is almost doubled compared to NiSA. To the best of our knowledge, this result outperforms most, if not all, CO₂-to-CO catalysts in H-cells reported to date (Table S3). The Faradic efficiency of CO (FE_{CO}) is shown in Fig. S10, where NiSA/NP can achieve an ultra-high FE_{CO} above 99% at -0.8 V. Besides, the onsite potential of NiSA/NP is at around -0.5 V vs RHE, which is approaching to the values predicted from DFT calculation on 2 e⁻ negatively charged NiN₃V model. The electrochemically active surface area (ECSA) is evaluated from double-layer capacitance (C_{dl}) to elucidate the origin of the enhanced catalytic activity on NiSA/NP (Fig. S11).³⁶ The NiSA/NP shows slightly higher C_{dl} compared with NiSA (1.4 mF vs 1.2 mF), suggesting that the improved catalytic activity is primarily attributed to the intrinsic reactivity of each site, rather than a surface area effect (Fig. 3b). Stability testing is then performed at -0.75 V vs RHE, NiSA/NP shows robust durability for CO₂RR during 30 hours of continuous electrolysis, maintaining constant current densities and 99% of the initial FE for CO production (Fig. 3c). This can be attributed to the strong immobilization and close proximity between catalysts and CNTs, which reduce aggregation and bypass undesired side reactions to suppress catalyst deactivation.³⁷

To assess the performance of catalysts at industrial-relevant devices and current densities, we further evaluate the CO₂RR in flow cells using gas diffusion electrodes (Fig. S12). Figure 4a displays the CO FEs and partial current densities plotted against the *iR*-corrected potentials in 1 M KOH flow cells. The NiSA/NP shows a low onsite potential at around -0.25 V vs RHE. Then, the CO partial currents quickly increase to above 200 mA cm⁻² at -0.4 V with FE_{CO} of 96%, and further reach 346 mA cm⁻² at -0.5 V with FE_{CO} of 98%. As a comparison, the highest current obtained with NiSA is 263 mA cm⁻² at -0.65 V (Fig. S13). The superior CO₂RR performance of NiSA/NP in the flow cell can be attributed to (i) the

significantly enhanced CO₂ mass transport based on gas diffusion electrode and (ii) the catalytic promotion effect in alkaline electrolytes.⁴³

The full cell performance was then tested based on the zero-gap MEA device, which is regarded as a promising prototype for practical application because of the very low cell resistance and robust structure. Figure 4b exhibits the LSV curves of two different full cells by using IrO₂ and NiFe anodes, respectively. With 1 M KOH as the anolyte, the NiSA/NP@NiFe cell shows even better performance than the widely used IrO₂ anode. It is worth noting that the Ir-based anode can cost more than 60% of the total price of MEA device,⁷ so that the development of the low-cost substitution is highly desirable. As shown in Fig. 4c, the NiSA/NP@NiFe cell delivers a j_{CO} of 163 mA cm⁻² with FE_{CO} of 92% at -2.0 V without iR compensation. With further increase of cell voltage to -2.3 V, the j_{CO} can reach up to 310 mA cm⁻² with FE_{CO} of ~99%, corresponding to an outstanding full cell energy efficiency of 57% based on the calculation: $EE = \Delta E^0 / \Delta E^{\text{Applied}} \times FE_{\text{CO}}$, where EE is the energy efficiency, ΔE^0 is the equilibrium full cell voltage ($E^0_{\text{CO}} - E^0_{\text{OER}} = -0.11 \text{ V} - 1.23 \text{ V} = -1.34 \text{ V}$), and $\Delta E^{\text{Applied}}$ is the applied full cell voltage without iR -correction. Note that certain Ag-based MEA devices can achieve current densities above 600 mA cm⁻² but at a much higher cell voltage of -3.5 V with a low energy efficiency of ~35%.³⁸ In comparison, our NiSA/NP@NiFe cell shows the highest energy efficiency and the lowest cell voltage ever reported for CO production at an industrially relevant current of ~300 mA cm⁻² (Fig. 4d and Table S4).

Discussion

In conclusion, a cooperative Ni SAC via nanoparticles coupling was firstly designed by DFT modelling, which showed electron enrichment of single-Ni-sites with enhanced binding to the key intermediate COOH*. The promotion effect of Ni nanoparticles was pursued experimentally by the solid-state pyrolysis with excessive Ni sources. Extensive structural characterizations revealed a low valence of Ni single atom with abundant unpaired d-electrons in the structure. As such, the greatly enhanced CO₂RR activity on NiSA/NP is understood as a result of its tuned electronic configuration. Together with the populated Ni single atom (4.6 wt%), a state-of-the-art performance is achieved in the MEA full cell, which delivered a high CO current of 310 mA cm⁻² at -2.3 V with an overall energy efficiency of 57%. We believe this Ni SACs that rivalled nanostructured Au and Ag could accelerate the industrial implementation of energy-efficient CO₂RR. The proof-of-concept also opens a new avenue for the design of cooperative SACs, which can potentially break the linear scaling relationship for a range of technologically important catalytic reactions.

Methods

Synthesis of NiSA/NP catalyst. 0.3 g of Ni(NO₃)₂·6H₂O and 3 g of melamine were manually ground for 10 min to get the uniform light-green solid precursor. It was then annealing in the tube furnace in Ar

atmosphere at 1000°C for 2h with a heating rate of 5°C min⁻¹. The final NiSA/NP catalyst can be obtained by washing the sintered powder with 3 M HCl and H₂O to remove the impurities.

Synthesis of NiSA catalyst. The NiSA catalyst was prepared by the NH₄Cl treatment method.³² Namely, 0.1 g of NiSA/NP and 3 g of NH₄Cl were manually ground for 10 min to get the uniform black precursor. It was then annealing in the tube furnace in Ar atmosphere at 1000°C for 2h with a heating rate of 5°C min⁻¹. The final NiSA catalyst can be obtained by washing the sintered powder with 3 M HCl at 80°C and H₂O to remove the impurities.

Characterizations. Scanning electron microscope (SEM) images were collected with a QUANTA 450. Transmission electron microscopy (TEM), high-resolution TEM (HRTEM), high angle annular dark-field scanning TEM (HAADF-STEM) were carried out on JEOL JEM-ARM200f microscope at 200 kV. XRD was performed on a PANalytical X'Pert X-ray diffraction system (45 kV, 40 mA, Cu K α radiation). XPS results were recorded by Thermo ESCALAB250Xi. XAFS spectra at the Ni K-edge were collected in the Australia Synchrotron center in fluorescence mode. EPR spectra were conducted on a benchtop spectrometer Bruker EMXnano with x band.

Electrochemical measurements. CO₂ electrolysis in H-cells was performed in a gas-tight H-cell with two compartments separated by a cation exchange membrane (Nafion®117). A Pt plate was used as the counter electrode, a saturated calomel electrode (SCE) was used as the reference electrode, and CO₂-saturated 0.5 M KHCO₃ was used as the electrolyte, respectively. To prepare the working electrodes, 10 mg of catalyst and 100 μ L of 5% Nafion solution were introduced into 100 μ L of water and 300 μ L of ethanol solution and sonicated for 1 h. A 6.25 μ L of the catalyst ink was coated onto a carbon fiber paper substrate and dried in the air, giving an effective area of 0.25 cm⁻² with catalyst loading of 0.5 mg cm⁻². In H-cells, LSV and potentiostatic data were corrected with an *iR* compensation of 80%.

CO₂ electrolysis in flow cells. The windows for electrolysis were set to 1 cm \times 1 cm. Each chamber has an inlet and an outlet for electrolyte, and an Ag/AgCl reference electrode was placed in the catholyte chamber. The catalyst ink was prepared by mixing 10 mg of catalyst, 3 mL of ethanol and 100 μ L of a Nafion perfluorinated resin solution. Then, catalysts were air-brushed onto 3 \times 3 cm⁻² 38 BC gas diffusion layer (FuelCellStore) electrodes and used as the cathode. Commercial IrO₂ sprayed on Titanium mesh was used as a counter electrode for oxygen evolution reaction (OER). An anion exchange membrane (FAA-3-50, FuelCellStore) was used to separate the cathode and anode chambers. 1 M KOH solution was used as the electrolytes. The catholyte and anolyte were cycled at a flow rate of 10 mL min⁻¹ by using a peristaltic pump. LSV and potentiostatic data were corrected with an *iR* compensation of 80%.

CO₂ electrolysis in zero-gap MEA device. The windows for electrolysis were set to 1 cm⁻². Cathode and anode chambers have an inlet and an outlet for gas and electrolyte, respectively. Both the cathode and

perfluorinated resin solution. Then, the cathode catalyst was air-brushed onto $3 \times 3 \text{ cm}^{-2}$ 38 BC gas diffusion layer (FuelCellStore) electrodes, and the anode catalyst was air-brushed onto $3 \times 3 \text{ cm}^{-2}$ 35 AA carbon paper (Ion Power) electrodes. The anode NiFe catalysts were prepared by our previously reported method.^{44,45} An Sustainion® X37-50 was used as the membrane. The cathode was feed with humidified CO₂ gas and the anode was feed with 1 M KOH electrolytes. The applied cell voltages were recorded without *iR* correction.

Declarations

Acknowledgments

This work was supported by the Australian Research Council (FT170100224, DP210103892). The authors are thankful to Dr. Jun Gu for his help in the assembly of flow cell and membrane electrolyser, and Australia Synchrotron center (ANSTO), and UNSW Mark Wainwright Analytical Center for providing access to their XAFS, XRD, SEM, XPS, NMR and facilities. This research was also undertaken with the assistance of resources provided by the National Computing Infrastructure (NCI) facility at the Australian National University; allocated through both the National Computational Merit Allocation Scheme supported by the Australian Government and the Australian Research Council grant LE190100021 (Sustaining and strengthening merit-based access at NCI, 2019-2021). This project has received funding from the European Union's Horizon 2020 research and innovation programme under the Marie Skłodowska-Curie grant agreement (891545-ADBCRZB). The work is part of NCCR Catalysis, a National Centre of Competence in Research funded by the Swiss National Science Foundation.

Author Contributions

C.Z. and X.H. directed the project. W.R. designed the experiments, analyzed the results and wrote the first draft of the manuscript. X.T. and S.S. performed the DFT calculation. C.J. and Q.S. carried out the XAS experiments and data analysis. A.K. and A.S. performed the UPS testing. J.Q. conducted the TEM characterizations. All authors contribute to the writing of the manuscript.

Competing interests

C.Z., W. R., and Q.S. are filing an Australian provisional patent based on this research.

Additional information

Supplementary information is available for this paper.

References

- 1 Ross, M. B. *et al.* Designing materials for electrochemical carbon dioxide recycling. *Nat. Catal.* **2**, 648-659 (2019).

Loading [MathJax]/jax/output/CommonHTML/jax.js

- 2 Jin, S., Hao, Z., Zhang, K., Yan, Z. & Chen, J. Advances and Challenges for Electrochemical Reduction of CO₂ to CO: From Fundamental to Industrialization. *Angew. Chem. Int. Ed.* (2021), doi.org/10.1002/anie.202101818.
- 3 Kibria, M. G. *et al.* Electrochemical CO₂ Reduction into Chemical Feedstocks: From Mechanistic Electrocatalysis Models to System Design. *Adv. Mater.* **31**, 1807166 (2019).
- 4 Diercks, C. S., Liu, Y., Cordova, K. E. & Yaghi, O. M. The role of reticular chemistry in the design of CO₂ reduction catalysts. *Nat. Mater.* **17**, 301-307, (2018).
- 5 Ren, W. & Zhao, C. Paths towards enhanced electrochemical CO₂ reduction. *Nati. Sci. Rev.* **7**, 1-9, (2019).
- 6 Zhong, M. *et al.* Accelerated discovery of CO₂ electrocatalysts using active machine learning. *Nature* **581**, 178-183 (2020).
- 7 Masel, R. I. *et al.* An industrial perspective on catalysts for low-temperature CO₂ electrolysis. *Nat. Nanotechnol.* **16**, 118-128 (2021).
- 8 Krause, R. *et al.* Industrial application aspects of the electrochemical reduction of CO₂ to CO in aqueous electrolyte. *Chem. Ing. Tech.* **92**, 53-61 (2020).
- 9 Zhao, S., Jin, R. & Jin, R. Opportunities and challenges in CO₂ reduction by gold-and silver-based electrocatalysts: From bulk metals to nanoparticles and atomically precise nanoclusters. *ACS Energy Lett.* **3**, 452-462 (2018).
- 10 Yin, Z. *et al.* An alkaline polymer electrolyte CO₂ electrolyzer operated with pure water. *Energy Environ. Sci.* **12**, 2455-2462 (2019).
- 11 Li, M. *et al.* Heterogeneous Single-Atom Catalysts for Electrochemical CO₂ Reduction Reaction. *Adv. Mater.* **32**, 2001848 (2020).
- 12 Gu, J., Hsu, C.-S., Bai, L., Chen, H. M. & Hu, X. Atomically dispersed Fe³⁺ sites catalyze efficient CO₂ electroreduction to CO. *Science* **364**, 1091-1094 (2019).
- 13 Yang, H. *et al.* Carbon dioxide electroreduction on single-atom nickel decorated carbon membranes with industry compatible current densities. *Nat. Commun.* **11**, 1-8 (2020).
- 14 Jiao, J. *et al.* Copper atom-pair catalyst anchored on alloy nanowires for selective and efficient electrochemical reduction of CO₂. *Nat. Chem.* **11**, 222-228 (2019).
- 15 Pérez-Ramírez J, López N. Strategies to break linear scaling relationships. *Nat. Catal.* **2**, 971-976 (2020).

- 16 Ren, W, *et al.* Isolated Diatomic Ni-Fe Metal-Nitrogen Sites for Synergistic Electroreduction of CO₂. *Angew. Chem. Int. Ed.* **58**, 6972-6976 (2019).
- 17 Liu, *et al.* Elucidating the Electrocatalytic CO₂ Reduction Reaction over a Model Single-Atom Nickel Catalyst. *Angew. Chem. Int. Ed.* **59**, 798-803 (2020).
- 18 Deng, J., Deng, D. & Bao, X. Robust catalysis on 2D materials encapsulating metals: concept, application, and perspective. *Adv. Mater.* **29**, 1606967 (2017).
- 19 Dahal, A., & Batzill, M. Graphene–nickel interfaces: a review. *Nanoscale* **6**, 2548 (2014).
- 20 Gong, J., Wang, L., Liu, Y., Yang, J. & Zong, Z. Structural and magnetic properties of hcp and fcc Ni nanoparticles. *J. Alloys Compd.* **457**, 6-9 (2008).
- 21 Li, X. *et al.* Exclusive Ni-N₄ Sites Realize Near-Unity CO Selectivity for Electrochemical CO₂ Reduction. *J. Am. Chem. Soc.* **139**, 14889-14892, (2017).
- 22 Yan, C. *et al.* Coordinatively unsaturated nickel-nitrogen sites towards selective and high-rate CO₂ electroreduction. *Energy Environ. Sci.* **11**, 1204-1210 (2018).
- 23 Koshy, D. M. *et al.* Understanding the origin of highly selective CO₂ electroreduction to CO on Ni, N-doped carbon catalysts. *Angew. Chem.* **132**, 4072-4079 (2020).
- 24 Kortlever, R., Shen, J., Schouten, K. J. P., Calle-Vallejo, F. & Koper, M. T. Catalysts and reaction pathways for the electrochemical reduction of carbon dioxide. *J. Phys. Chem. Lett.* **6**, 4073-4082 (2015).
- 25 Kim, D. *et al.* Electrochemical activation of CO₂ through atomic ordering transformations of AuCu nanoparticles. *J. Am. Chem. Soc.* **139**, 8329-8336 (2017).
- 26 Shi, C., Hansen, H. A., Lausche, A. C. & Nørskov, J. K. Trends in electrochemical CO₂ reduction activity for open and close-packed metal surfaces. *Phys. Chem. Chem. Phys.* **16**, 4720-4727 (2014).
- 27 Dante, R. C., Martín-Ramos, P., Correa-Guimaraes, A. & Martín-Gil, J. Synthesis of graphitic carbon nitride by reaction of melamine and uric acid. *Mater. Chem. Phys.* **130**, 1094-1102 (2011).
- 28 Meng, J. *et al.* General oriented formation of carbon nanotubes from metal-organic frameworks. *J. Am. Chem. Soc.* **139**, 8212-8221 (2017).
- 29 Zhao, C. *et al.* Solid-diffusion synthesis of single-atom catalysts directly from bulk metal for efficient CO₂ reduction. *Joule* **3**, 584-594 (2019).
- 30 Qu, Y. *et al.* Direct transformation of bulk copper into copper single sites via emitting and trapping of atoms. *Nat. Catal.* **1**, 781-786 (2018).

- 31 Chen, M. X. *et al.* Identification of Catalytic Sites for Oxygen Reduction in Metal/Nitrogen-Doped Carbons with Encapsulated Metal Nanoparticles. *Angew. Chem. Int. Ed.* **59**, 1627-1633 (2020).
- 32 Yang, H. B. *et al.* Atomically dispersed Ni (I) as the active site for electrochemical CO₂ reduction. *Nat. Energy* **3**, 140 (2018).
- 33 Wongnate, T. *et al.* The radical mechanism of biological methane synthesis by methyl-coenzyme M reductase. *Science* **352**, 953-958 (2016).
- 34 Hammer, B. & Nørskov, J. K. Theoretical surface science and catalysis—calculations and concepts. *Adv. Catal.* **45**, 71-129 (2000).
- 35 Zhang, T. *et al.* Atomically Dispersed Nickel (I) on an Alloy-Encapsulated Nitrogen-Doped Carbon Nanotube Array for High-Performance Electrochemical CO₂ Reduction Reaction. *Angew. Chem.* **132**, 12153-12159 (2020).
- 36 Voiry, D. *et al.* Best practices for reporting electrocatalytic performance of nanomaterials. *ACS Nano* **12**, 9635-9638 (2018).
- 37 Hu, X. M., Rønne, M. H., Pedersen, S. U., Skrydstrup, T. & Daasbjerg, K. Enhanced catalytic activity of cobalt porphyrin in CO₂ electroreduction upon immobilization on carbon materials. *Angew. Chem. Int. Ed.* **56**, 6468-6472 (2017).
- 38 Endrődi, B. *et al.* Operando cathode activation with alkali metal cations for high current density operation of water-fed zero-gap carbon dioxide electrolyzers. *Nat. Energy* **6**, 439-448 (2021).
- 39 Jiang, K. *et al.* Isolated Ni single atoms in graphene nanosheets for high-performance CO₂ reduction. *Energy Environ. Sci.* **11**, 893-903 (2018).
- 40 Zheng, T. *et al.* Large-scale and highly selective CO₂ electrocatalytic reduction on nickel single-atom catalyst. *Joule* **3**, 265-278 (2019).
- 41 Jeong, H.-Y. *et al.* Achieving highly efficient CO₂ to CO electroreduction exceeding 300 mA cm⁻² with single-atom nickel electrocatalysts. *J. Mater. Chem. A* **7**, 10651-10661 (2019).
- 42 Ren, S. *et al.* Molecular electrocatalysts can mediate fast, selective CO₂ reduction in a flow cell. *Science* **365**, 367-369 (2019).
- 43 Dinh, C.-T. *et al.* CO₂ electroreduction to ethylene via hydroxide-mediated copper catalysis at an abrupt interface. *Science* **360**, 783-787 (2018).
- 44 Song, F. *et al.* An unconventional iron nickel catalyst for the oxygen evolution reaction. *ACS Cent. Sci.* **5**, 558-568 (2019).

Figures

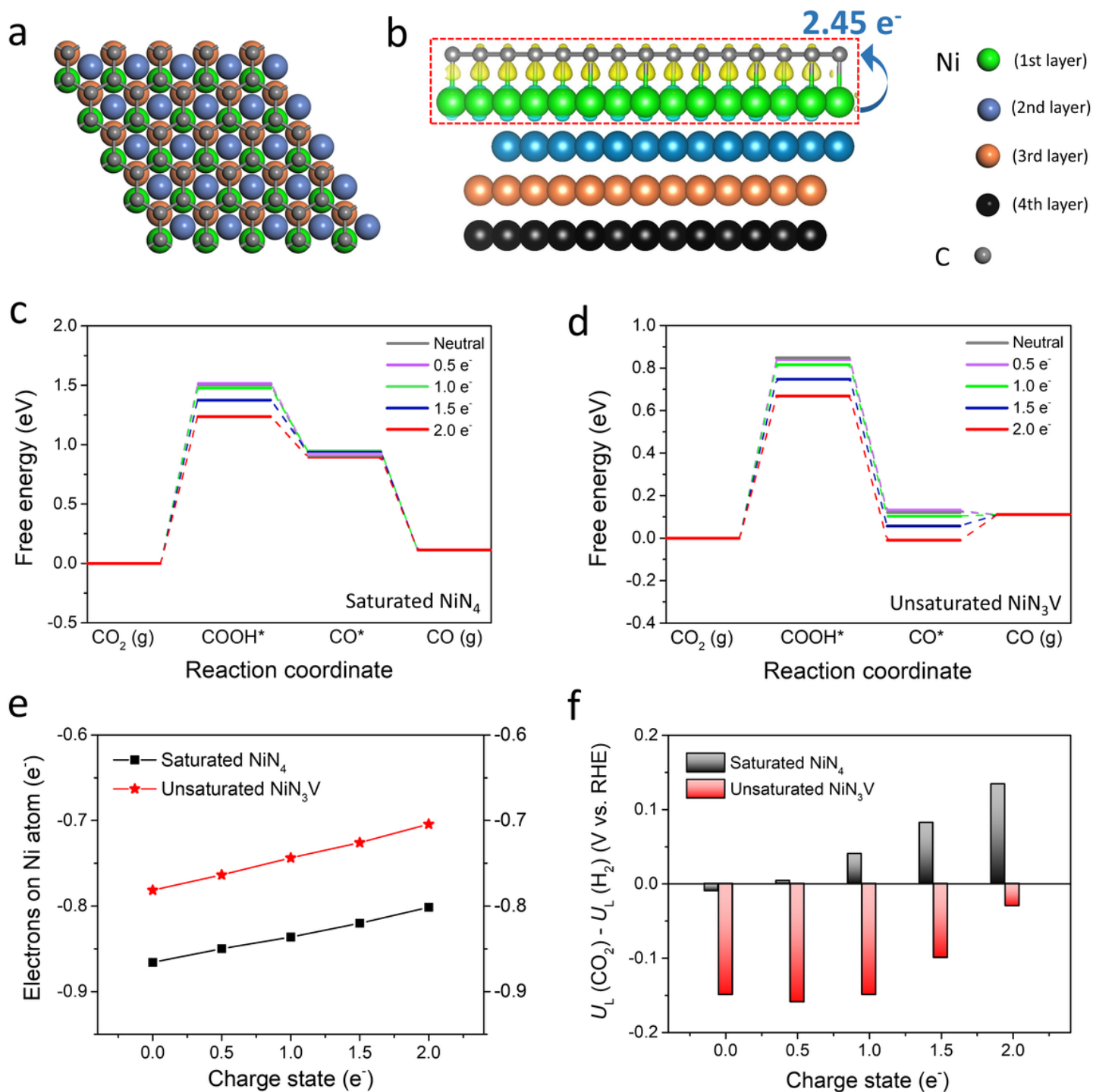


Figure 1

Density functional theory (DFT) calculation. (a) Top view of the optimized structures of Ni(111)/graphene. (b) Information electronic density of the Ni(111)/graphene. The

calculated free energy diagrams for CO₂RR to CO on neutral and negatively charged NiN₄V (c) and NiN₃V (d), respectively. (e) The number of electrons on Ni single atom in neutral and negatively charged Ni-N-C structures. (f) Difference in limiting potentials for CO₂ reduction and H₂ evolution on neutral and negatively charged Ni-N-C.

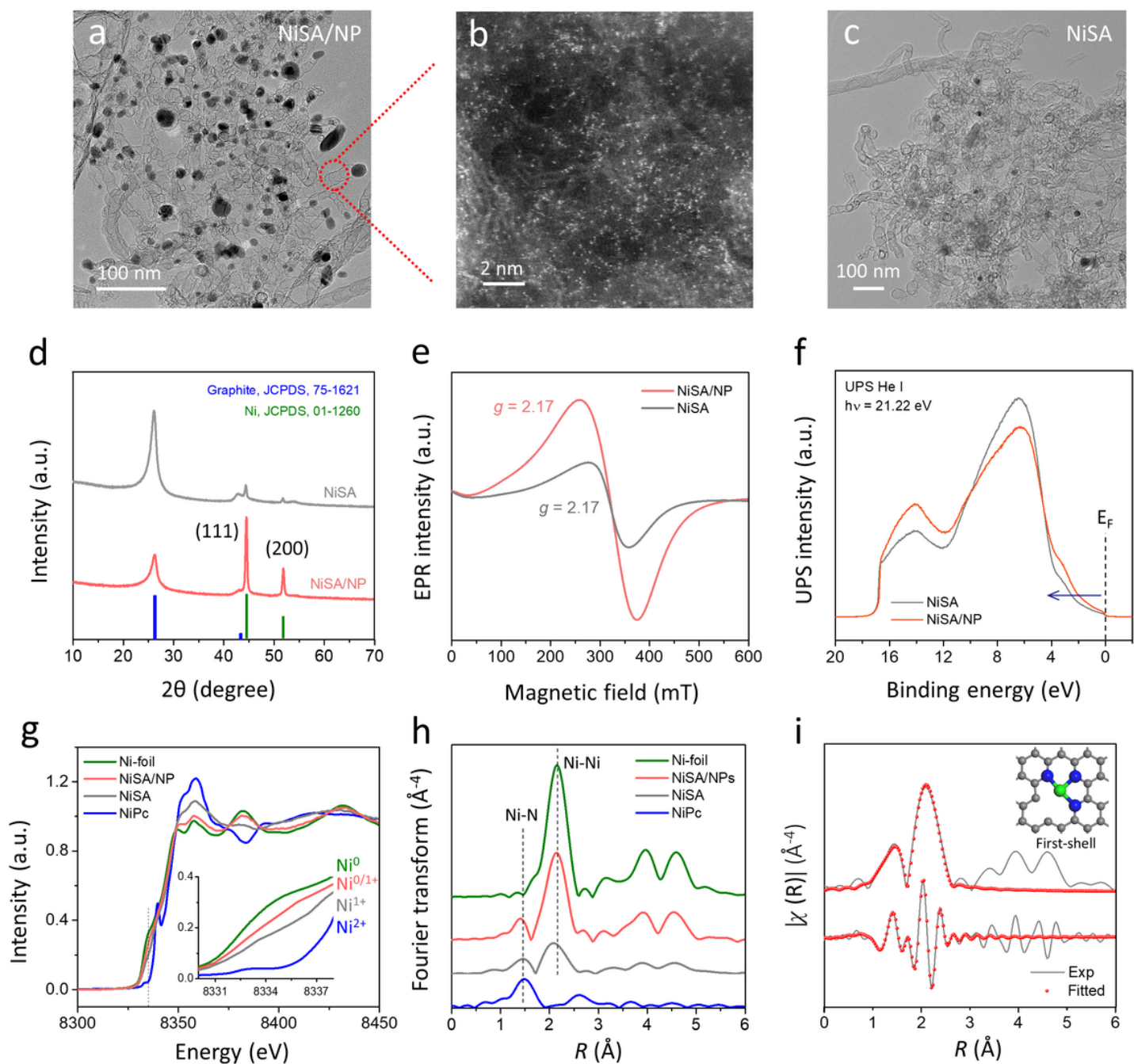


Figure 2

Materials characterizations. (a) Transmission electron microscopy (TEM) image of NiSA/NP. (b) High-angle annular dark-field scanning transmission electron microscopy (HAADF-STEM) image of NiSA/NP. (c) TEM image of NiSA. (d) X-ray diffraction results. (e) Electron paramagnetic resonance (EPR) spectra measured at 292 K. (f) UPS He I spectra of NiSA/NP and NiSA. (g) Ni K-edge XANES spectra of NiSA/NP

Loading [MathJax]/jax/output/CommonHTML/jax.js

and NiSA with the comparison of standard NiPc and Ni foil. The inset shows the enlarged pre-edge region. (h) The plotted Fourier transformation of extended X-ray absorption fine structure (FT-EXAFS) spectra of NiSA/NP, NiSA, Ni-foil, and NiPc. (i) EXAFS fitting of NiSA.

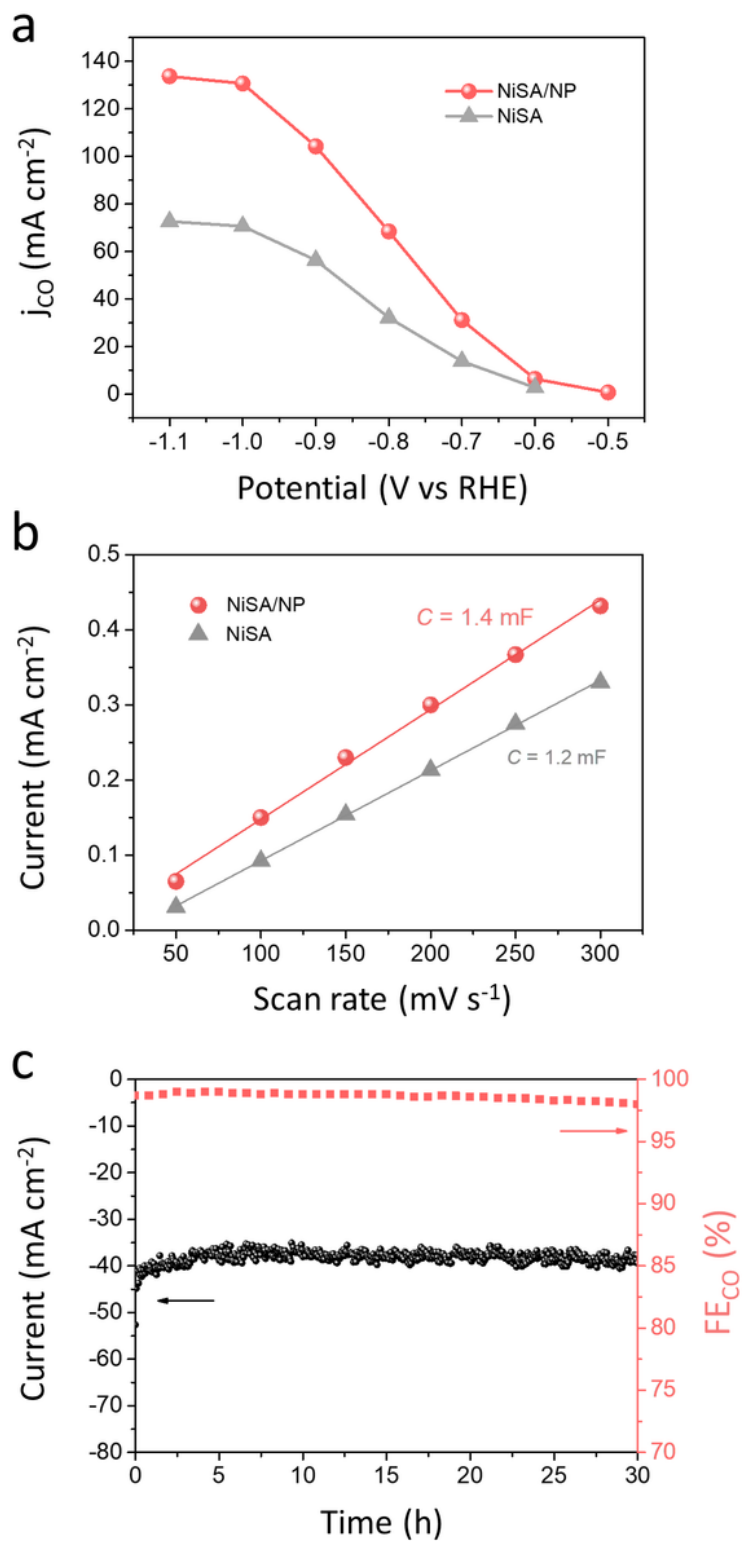


Figure 3

CO₂RR in H-cells. (a) Partial CO currents plotted against different potentials. (b) Double-layer capacitance loading [MathJax]/jax/output/CommonHTML/jax.js ng at -0.75 V vs. RHE for 30 h electrolysis.

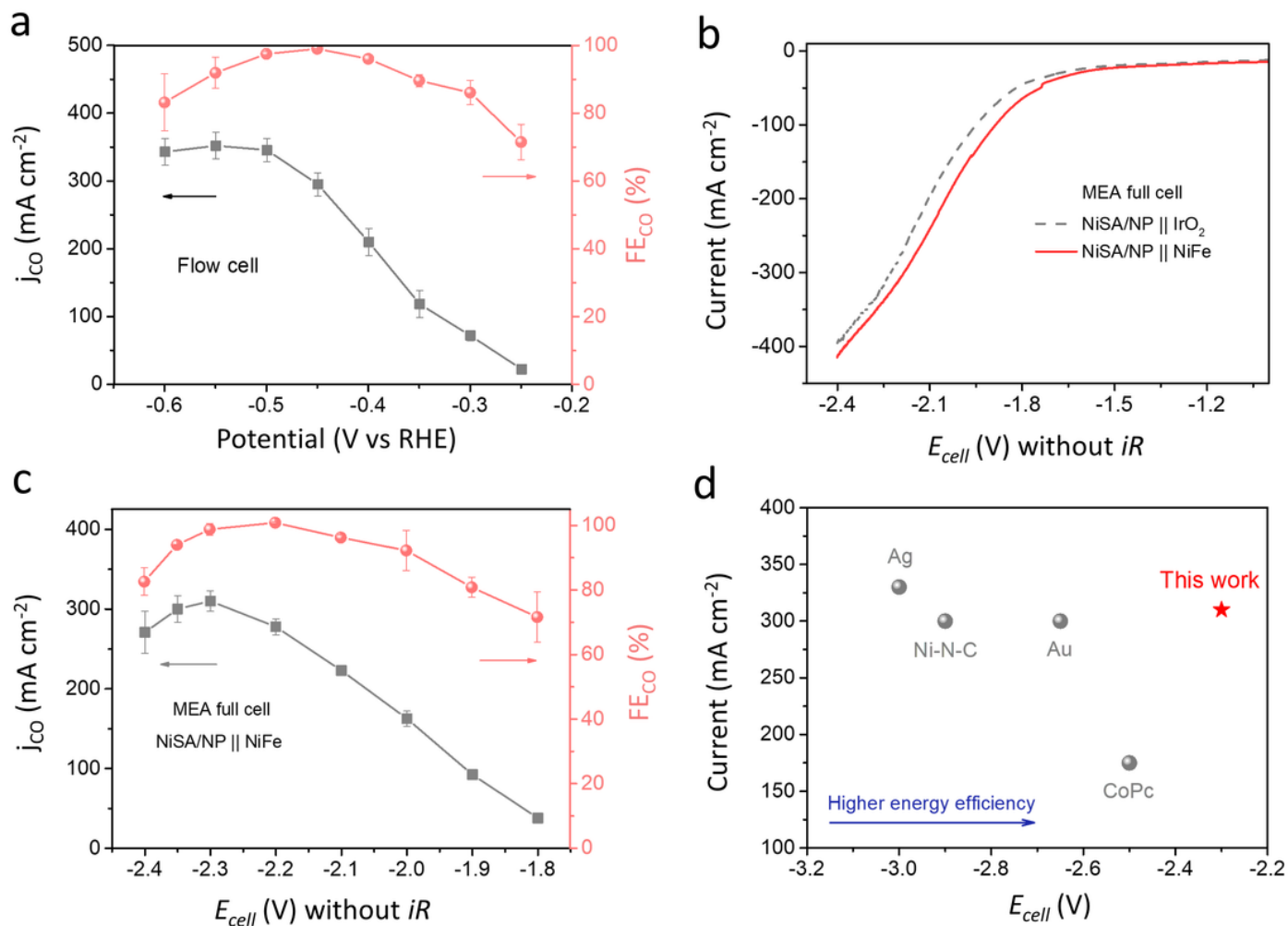


Figure 4

Gas diffusion electrode-based devices for CO₂RR. (a) j_{CO} and FE_{CO} at different potentials in 1 M KOH flow cells. (b) Polarisation curves obtained at a scan rate of 10 mV s⁻¹ in the zero-gap MEA full cells with IrO₂ and NiFe as the anode, and 1 M KOH as the electrolyte. (c) j_{CO} and FE_{CO} as functions of overall NiSA/NP || NiFe cell voltages from -1.8 V to -2.3 V. (d) Comparison of the state-of-the-art Au, Ag, Ni-N-C and CoPc catalysts in MEA electrolyser.

Supplementary Files

This is a list of supplementary files associated with this preprint. Click to download.

- [SupportingInformation.docx](#)